Journal of Metals, Materials and Minerals, 36(2), e2508, 2026

Finite element simulation of surface repair welding of grade R260 railway rails using thermite welding

Werayoot LAHAMORNCHAIYAKUL[1], Saksit CHUENCHOMNAKJAD[1], Thongchai KHRUEAPHUE[2,*] and Parinyawatr DHINNABUTRA[3]

[1] *Faculty of Engineering, Rajamangala University of Technology Lanna Phitsanulok, Mueang Phitsanulok, 65000, Thailand*
[2] *Program in Industrial Engineering Technology and Logistics, Faculty of Agricultural and Industrial Technology, Phetchabun Rajabhat University, 67000, Thailand*
[3] *Faculty of Technical Education, Rajamangala University of Technology Isan, Khon Kaen, 40000, Thailand*

***Corresponding author e-mail**: Thongchai.k@pcru.ac.th

Received date:
18 September 2025
Revised date:
8 January 2026
Accepted date:
17 April 2026

Keywords:
Thermite welding;
Railway rail repair;
Finite element simulation;
Mold design;
R260 rail steel

Abstract

Railway rails subjected to repetitive wheel-rail contact loads experience surface damage, including shallow cracks, groove wear, and material loss. Conventional arc welding repair presents limitations in costs, repair time, and quality consistency. This study investigates thermite welding for surface repair of pearlitic rail steel grade R260, emphasizing the effects of mold overflow configuration on thermal behavior, molten metal flow, and weld quality. A finite element framework incorporating thermal-fluid coupling was developed to simulate temperature distribution and molten metal penetration. Three mold overflow configurations were evaluated: overflow at the wear groove outer edge (Case 1), near the pouring gate (Case 2), and above the pouring gate (Case 3). The Herschel-Bulkley model captured yield-controlled flow and shear-thinning behavior of molten thermite steel. Numerical predictions were validated experimentally. Case 1 achieved a 1620°C peak temperature with shallow heat dispersion, causing incomplete fusion. Case 2 reached 1750°C to 1800°C but exhibited porosity from unbalanced flow. Case 3 demonstrated optimal performance: 1880°C peak temperature, uniform thermal distribution, complete groove filling, and minimal defects. Microstructural examination confirmed dense welds with negligible porosity meeting ISO 5817 standards. Strong correlation between numerical and experimental results validates the modeling framework, demonstrating that mold overflow geometry critically governs heat transfer, flow stability, and weld integrity. Case 3 represents the optimal configuration for thermite-based rail surface repair, providing practical design guidance for improving repair efficiency in railway maintenance operations.

1. Introduction

Railway systems represent a critical component of transportation infrastructure, playing a vital role in economic development and mobility. This aligns with Thailand's 20-Year National Strategy (2018–2037), particularly Strategy 2: National Competitiveness Enhancement, which emphasizes the development of infrastructure and logistics systems to support sustainable economic growth. Railway rails are subjected to repetitive wheel–rail contact loads under real service conditions, which gradually induce material degradation [1]. Surface-related damage, including shallow cracks, groove wear, and localized material loss, is frequently observed in the rail head region, where direct contact with train wheels occurs. If such damage is not properly addressed through timely maintenance, it may progressively develop into structural deterioration and compromise operational safety [1,2]. Although full rail replacement provides a permanent solution, it requires extended service interruptions and incurs substantial costs. Consequently, localized rail surface repair has become a more practical and economically viable approach in railway maintenance operations [3,4]. Conventional rail surface repair is commonly performed using arc welding overlay techniques [5]. While these methods can restore surface geometry to some extent, they are associated with several limitations, including high operational costs, prolonged repair time, complex procedures, and variability in weld quality under field conditions. These limitations are particularly pronounced when repairing shallow and irregular surface defects, where precise control of heat input and molten metal penetration is difficult to achieve [6]. As a result, there is growing interest in alternative repair techniques that offer simplified procedures, reduced material consumption, and improved process controllability.

Thermite welding has been widely applied in railway maintenance, particularly for rail joint welding, due to its ability to generate extremely high temperatures through an aluminothermic reaction without the need for external power sources. The reaction between aluminum powder and iron oxide produces molten steel at temperatures exceeding 2500°C, enabling effective melting and bonding with the parent rail material [4]. Compared with conventional arc welding techniques, thermite welding offers practical advantages such as

reduced equipment complexity, shorter repair duration, and lower maintenance costs [5]. While the process is well established for rail joint applications, its direct use for rail surface repair remains less explored and presents distinct engineering challenges. A key challenge in applying thermite welding to rail surface repair lies in controlling molten metal flow and heat transfer within shallow and confined surface defects [6]. Unlike rail joint welding, surface repair involves limited defect volume and rapid heat dissipation, which may restrict molten metal penetration and lead to premature solidification. In addition, the flow behavior, gas evacuation, and solidification characteristics of the molten thermite steel are strongly influenced by mold design, particularly the configuration and placement of overflow channels. Inappropriate mold geometry may result in defects such as porosity, incomplete fusion, and localized stress concentration, thereby reducing weld integrity and long-term performance [7].

In recent years, numerical simulation techniques based on Computational Fluid Dynamics (CFD) and the Finite Element Method (FEM) have been increasingly employed to investigate thermal–fluid phenomena in welding and casting processes. Previous studies have demonstrated the capability of numerical modeling to describe molten metal flow, temperature evolution, and solidification behavior in thermite and related high-temperature processes [8-10]. However, existing investigations have predominantly focused on rail joint welding or general thermite reactions [11], whereas studies specifically addressing thermite-based rail surface repair and the influence of mold overflow configuration remain limited. Moreover, systematic integration of numerical predictions with experimental validation in the context of surface repair applications has not been sufficiently reported [12].

In this context, the present study investigates the influence of mold overflow configuration on thermal behavior, molten metal flow, and weld quality during thermite-based surface repair of pearlitic rail steel grade R260 [13]. A finite element–based numerical framework incorporating thermal–fluid coupling was developed to simulate temperature distribution and molten metal penetration under different mold designs. The numerical results were validated through experimental thermite welding trials, including surface inspection and microstructural analysis. The findings provide insights into the role of mold design in controlling heat transfer and weld integrity and may support the optimization of thermite welding practices for rail surface repair applications. Although thermite welding has been extensively studied for rail joint applications, systematic investigations integrating thermal–fluid numerical modeling with experimental validation to evaluate mold overflow design for rail surface repair remain limited.

2. Experimental

2.1 Preparation of simulated rail surface wear

Figure 1 illustrates the preparation of a simulated surface wear defect on pearlitic rail steel grade R260 for experimental investigation. Typical surface damage observed under actual service conditions is shown in Figure 1(a), while the schematic representation and the fabricated specimen are presented in Figure 1(b-c), respectively. Field observations indicate that rail surface degradation is generally shallow and localized, resulting from rolling contact fatigue and abrasive wear.

To realistically represent such damage while maintaining precise control over geometric parameters, an artificial wear groove was machined on the rail surface. The groove had dimensions of 65 mm in length, 40 mm in width, and 5 mm in depth, closely matching typical field damage. An elliptical groove profile was selected to reproduce the stress concentration and wear morphology commonly observed on in-service rails. This artificial wear region served as the target zone for evaluating molten metal flow, penetration, and solidification behavior during thermite-based rail surface repair. The preparation of a controlled and repeatable wear geometry was essential for ensuring consistency between experimental observations and numerical simulations, thereby enabling systematic evaluation of mold design effects.

2.2 Mold design and overflow configuration

Figure 2 presents the mathematical model developed for analyzing molten metal flow during thermite welding on the rail surface. The model includes the rail substrate, wear groove, pouring gate, and overflow channels, allowing realistic representation of molten metal flow paths, heat transfer, and solidification behavior.

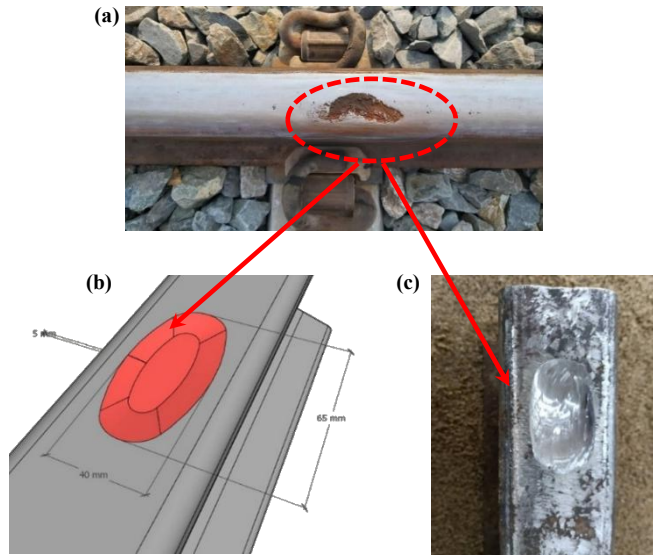

Figure 1. Preparation of simulated rail surface wear.

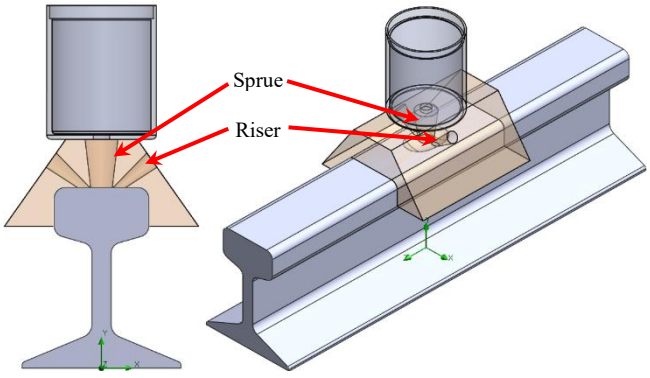

Figure 2. Mathematical model for molten metal flow analysis.

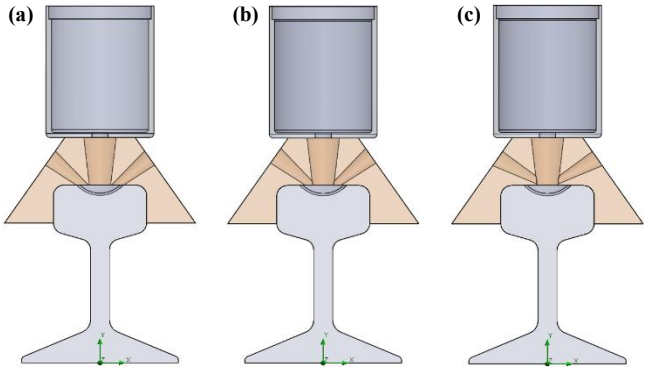

Figure 3. Mold overflow configurations: (a) overflow at outer edge of wear groove; (b) overflow near the pouring gate; (c) overflow positioned above the pouring gate.

Based on this framework, three mold overflow configurations were designed using SOLIDWORKS 2025, as illustrated in Figure 3. All designs employed a central pouring gate to ensure identical molten metal entry conditions, while the position of the overflow channel was varied to examine its influence on flow behavior and weld quality.

Design A, Figure 3(a). The overflow channel was positioned at the outer edge of the wear groove, allowing molten metal to discharge outward before fully filling the cavity.

Design B, Figure 3(b). The overflow channel was located adjacent to the pouring gate, providing partial control over flow direction and material distribution.

Design C, Figure 3(c). The overflow channel was positioned slightly above the pouring gate, promoting smooth and continuous downward-directed flow, reducing gas entrapment and porosity, and increasing filling density.

These configurations enabled comparative analysis of molten metal flow behavior, heat retention, and weld quality, providing engineering insight for optimizing thermite welding procedures for rail surface repair.

2.3 Governing equations and numerical formulation

The thermite welding process involves an intense aluminothermic reaction that generates molten steel at extremely high temperatures, followed by gravity-driven metal flow, heat transfer, and solidification within a confined mold. As a result, the process is governed by strongly coupled thermal-fluid phenomena involving molten metal flow, heat transfer, and phase transformation under high-temperature conditions [5,16]. In this study, the numerical model is formulated based on the fundamental conservation laws of mass, momentum, and energy to describe the post-reaction behavior of molten thermite steel [17]. The general mass conservation equation can be expressed as

$$\frac{\partial \rho}{\partial t} + \nabla \cdot (\rho u) = 0 \tag{1}$$

and for incompressible molten thermite steel with negligible density variation during mold filling, this equation reduces to

$$\nabla \cdot \mathrm{u} = 0 \tag{2}$$

Where u denotes the velocity vector [17,18]. Momentum transport of the molten thermite steel was governed by the transient incompressible Navier–Stokes equations [17,18].

$$\rho\left(\frac{\partial u}{\partial t} + \mathrm{u}\cdot\nabla\mathrm{u}\right) = -\nabla p + \nabla\cdot\left(\mu_{\mathrm{eff}}\nabla\mathrm{u}\right) + \rho g + S_{\mathrm{mushy}} \tag{3}$$

where gravitational acceleration represents the primary driving force for molten metal flow during thermite mold filling [14,16]. The source term S_{mushy} represents momentum damping induced by solidification and the formation of a mushy zone [18,19]. Energy conservation was formulated using an enthalpy-based approach to account for both sensible and latent heat effects during melting and solidification [17,18].

$$\frac{\partial(\rho H)}{\partial t} + \nabla\cdot(\rho \mathrm{u} H) = \nabla\cdot(k\nabla T) + S_{\mathrm{chem}} \tag{4}$$

Where H is the total enthalpy and S_{chem} denotes the volumetric heat source associated with the aluminothermic reaction [14,20]. Unlike arc welding or laser welding processes, no external electrical heat source or moving heat source formulation was applied in the present thermite welding model [15].

Melting and solidification were modeled using an enthalpy–porosity method, in which the liquid fraction f_L varies linearly between the solidus and liquidus temperatures, and the mushy zone is treated as a porous medium that progressively restricts molten metal flow [18,19]. The non-Newtonian behavior of molten thermite steel was described using the Herschel–Bulkley constitutive equation [21].

$$\tau = \tau_0 + K\dot{\gamma}^n \tag{5}$$

allowing accurate representation of yield-controlled flow initiation and shear-thinning behavior during gravity-driven mold filling [14,21].

2.4 Pre-processing and CFD simulation setup

2.4.1 Initial and boundary conditions

CFD simulations were conducted using SOLIDWORKS Flow Simulation 2025. The analysis type included fluid flow, heat conduction, and radiation effects. The ambient temperature was set to 35 °C to match experimental conditions. A transient simulation was performed with a total duration of 10 s and a time step of 0.01 s. Gravitational acceleration was applied as a body force in the negative vertical direction with a magnitude of 9.81 $\mathrm{m\cdot s^{-2}}$. Free-surface flow conditions were enabled to capture the dynamic molten metal–air interface during pouring and filling of the repair cavity.

2.4.2 Material properties for simulation

The thermophysical and rheological properties of the thermite material used for flow analysis are summarized in Table 1 molten thermite behavior was characterized using the Herschel–Bulkley constitutive model [21,22].

Table 1. Thermophysical and rheological properties of thermite used for flow analysis.

Properties	Variable	Unit
Density	6,750	$kg \cdot m^{-3}$
Specific heat	775	$J \cdot kg^{-1} \cdot K^{-1}$
Thermal conductivity	20	$W \cdot m^{-1} \cdot K^{-1}$
Viscosity	0.004	$Pa \cdot s^{-1}$
Yield stress [τ_0]	100	Pa
Consistency coefficient [K]	0.6	$Pa \cdot s^{-n}$
Power-law index [n]	0.3	N/A

Table 2. Thermophysical properties of CO_2 sand material used for mold.

Properties	Value	Unit
Density	1600	$kg \cdot m^{-3}$
Specific heat	1000	$J \cdot kg^{-1} \cdot K^{-1}$
Thermal conductivity	0.6	$W \cdot m^{-1} \cdot K^{-1}$
Coefficient of thermal expansion	5.8×10^{-6}	$1 \cdot K^{-1}$

Table 3. Thermophysical properties of rail steel grade R260.

Properties	Value	Unit
Density	7850	$kg \cdot m^{-3}$
Specific heat	470	$J \cdot kg^{-1} \cdot K^{-1}$
Thermal conductivity	50	$W \cdot m^{-1} \cdot K^{-1}$
Coefficient of thermal expansion	11.8×10^{-6}	$1 \cdot K^{-1}$

The model accounts for yield stress and flow resistance characteristics. A minimum yield stress of 100 Pa was required to initiate flow, with a power-law index of 0.3 indicating shear-thinning behavior. This rheological description is essential for accurately modeling flow initiation, propagation, and cavity filling during thermite welding. CO_2 sand was used as the mold material due to its thermal stability and ability to withstand high temperatures generated by the aluminothermic reaction [20,22]. Its thermophysical properties are listed in Table 2 [22].

The rail substrate material was pearlitic rail steel grade R260, with thermophysical properties provided in Table 3, which are critical for predicting solidification behavior and thermal stress development during welding [14]. The thermophysical properties were assumed to be temperature-independent. This simplification is justified by the short process duration (10 s) of the filling and initial solidification stage, during which the dominant thermal gradients occur over a narrow time window. Moreover, the primary objective of the present model is to capture the relative differences in flow behavior and heat distribution among the three mold configurations, rather than to predict absolute temperature values with high precision. This assumption is consistent with similar CFD studies of thermite and casting processes reported in the literature [8,22], and reduces numerical complexity while preserving the comparative validity of the model.

2.5 Wall boundary conditions

Wall boundary conditions were defined to represent realistic thermal–fluid interaction between molten thermite steel, mold surfaces, and the rail substrate. Partial slip conditions were implemented using parameters calibrated to capture yield-controlled flow and wall shear behavior, thereby improving the reliability of CFD predictions for molten metal flow during rail surface welding.

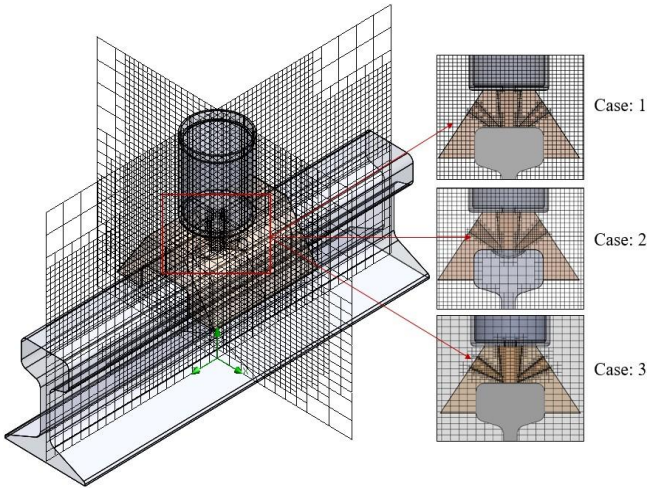

Figure 4. Mesh models employed in this study for the three overflow configurations.

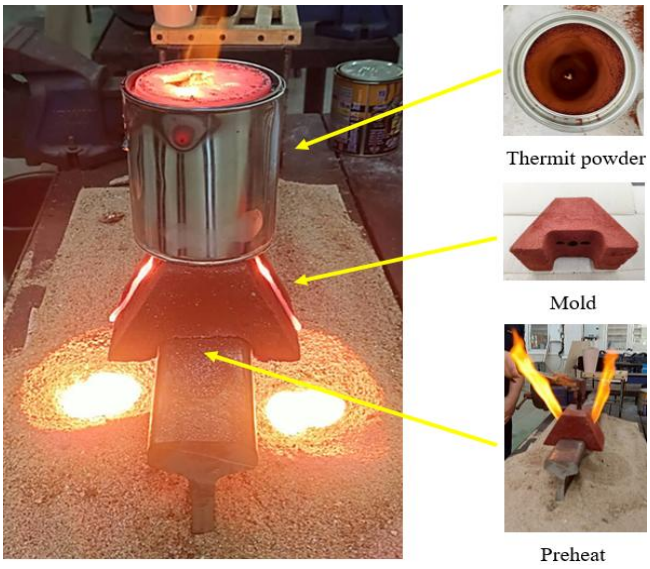

Figure 5. Experimental setup for rail surface repair welding.

Mesh generation employed local refinement in regions with high thermal and velocity gradients, particularly within the mold cavity, pouring gate, and fluid–solid interface zones. The refinement strategy ensured accurate resolution of heat transfer and flow behavior while maintaining computational efficiency. The final mesh consisted of approximately 5,440,162 elements and was verified to provide stable and mesh-independent results across all three mold configurations, as shown in Figure 4.

2.6 Experimental procedure for rail surface repair welding

Experimental thermite welding was conducted to validate the numerical predictions, as shown in Figure 5. The thermite mixture consisted of aluminum powder (Al) and iron oxide (Fe_2O_3), prepared and stored in sealed cylindrical containers prior to ignition. Welding molds were fabricated using silica sand, bentonite, graphite, sodium silicate, and water to ensure mechanical integrity and thermal resistance.

Prior to welding, the mold and rail surface were preheated using an oxy-acetylene flame to approximately 800°C for 5 min to reduce

thermal shock and improve molten metal wetting. The thermite charge was then ignited, producing reaction temperatures exceeding 2500°C. The molten steel reached temperatures of approximately 1600°C to 1900°C at the rail interface, enabling effective melting, infiltration, and defect filling.

After solidification, the mold was removed and excess material was mechanically trimmed. The repaired rail specimens were sectioned, polished, and etched for macroscopic and microstructural examination. Weld morphology, penetration depth, and defect formation were analyzed and compared with numerical predictions to validate the simulation framework.

3. Results and discussion

3.1 Thermal flow field analysis

The thermal flow field during thermite-based rail surface repair was analyzed using transient surface plots to visualize the coupled heat transfer and molten metal flow behavior within the rail specimen, mold, and molten metal domain. Figure 6 presents the simulated thermite reaction for three mold configurations (Case 1, Case 2, and Case 3) at time intervals of 2 s, 4 s, 6 s, 8 s, and 10 s, providing insight into the evolution of temperature distribution and molten metal infiltration.

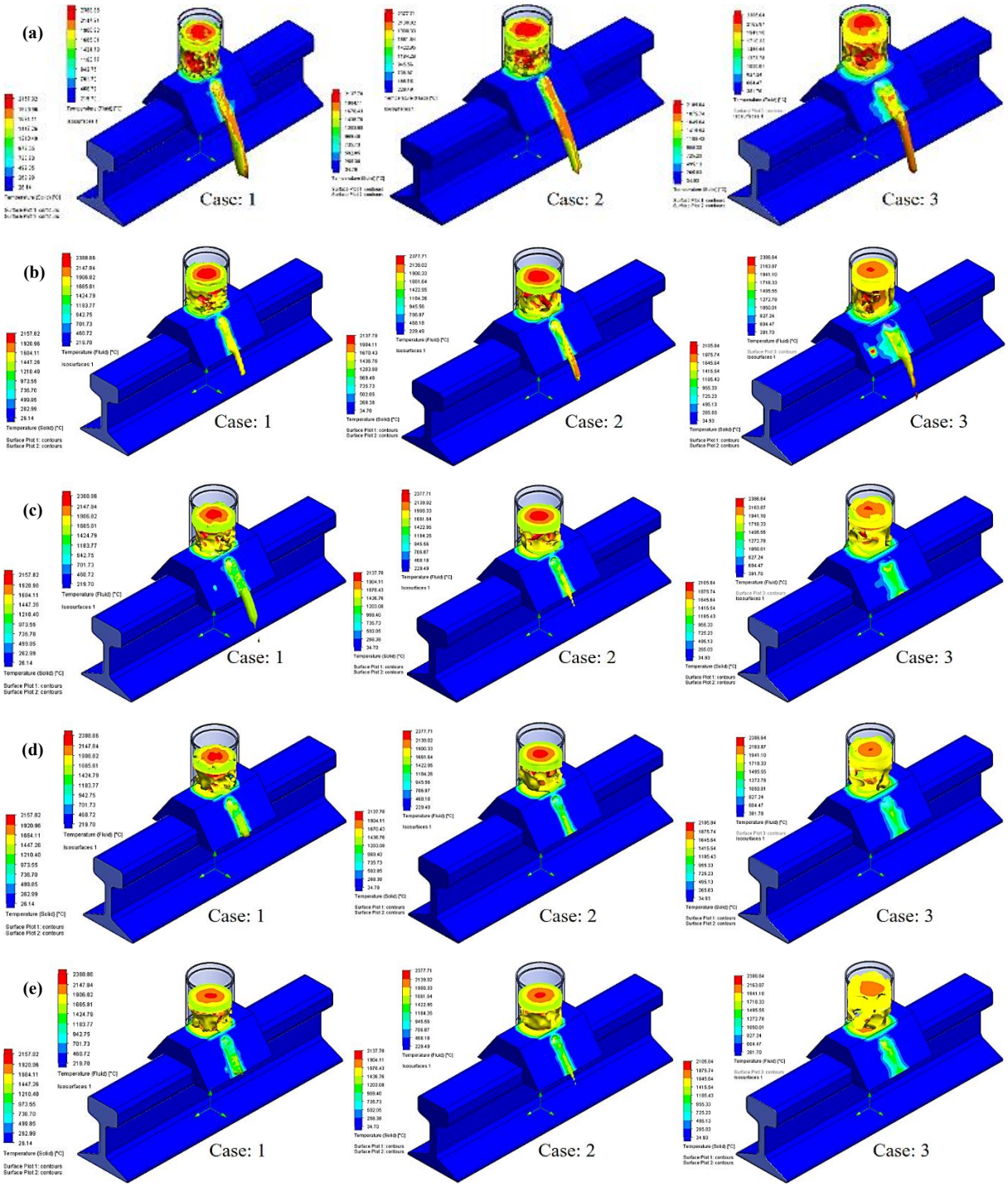

Figure 6. Simulated thermal flow of molten metal for three design cases at different time intervals: (a) 2 s, (b) 4 s, (c) 6 s, (d) 8 s, and (e) 10 s.

At 2 s is show in Figure 6(a), heat accumulation was primarily concentrated within the reaction chamber, with limited penetration into the mold cavity. Notably, Case 3 initiated molten metal flow earlier than the other configurations, indicating a more effective initial discharge path.

At 4–6 s is show in Figure 6(b-c), downward heat transfer and molten metal infiltration became more pronounced. Cases 2-3 exhibited improved flow continuity and enhanced mold–metal contact, whereas Case 1 retained a significant portion of thermal energy near the top of the chamber, delaying cavity infiltration.

At 8 s is show in Figure 6(d), most of the mold cavity was filled in all cases; however, Cases 2-3 displayed more uniform heat dispersion and smoother filling behavior, while Case 1 still exhibited localized thermal hotspots.

By 10 s is show in Figure 6(e), a complete thermal distribution was achieved in all configurations. Among them, Case 3 demonstrated the most homogeneous temperature field, confirming the effectiveness of its overflow design in promoting efficient molten metal distribution.

Overall, the results clearly indicate that mold overflow geometry plays a critical role in governing heat transfer and filling behavior during thermite welding. Case 3 provided the most uniform thermal field and complete mold filling, supporting its suitability for thermite-based rail surface repair.

3.2 Heat distribution on the rail surface

The temperature distribution within the rail substrate at 10 s was further examined to evaluate heat transfer from the thermite reaction into the rail surface. Figure 7 compares the temperature–distance profiles across the weld section for the three investigated cases.

Case 2 exhibited a peak temperature of approximately 1750°C to 1800°C, accompanied by the steepest and narrowest thermal gradient. This behavior indicates rapid and highly localized heating, which is advantageous for precision welding applications requiring controlled thermal input. In contrast, Case 1 showed a lower peak temperature of approximately 1620°C with a broader and shallower profile, resulting in limited heat penetration into the rail substrate and an increased risk of incomplete metallurgical bonding.

Case 3 reached the highest peak temperature, approaching 1880°C, and produced the broadest and deepest heat penetration profile. This thermal behavior demonstrates a superior capability to deliver heat widely and deeply into the rail, thereby promoting robust metallurgical fusion. In comparative terms, Case 2 is most suitable for localized, high-temperature applications, whereas Case 1 minimizes the heat-affected zone but is prone to insufficient fusion. Case 3 achieved comprehensive heat penetration and exhibited the strongest bonding potential, making it the most effective confraction for thermite-based rail surface repair.

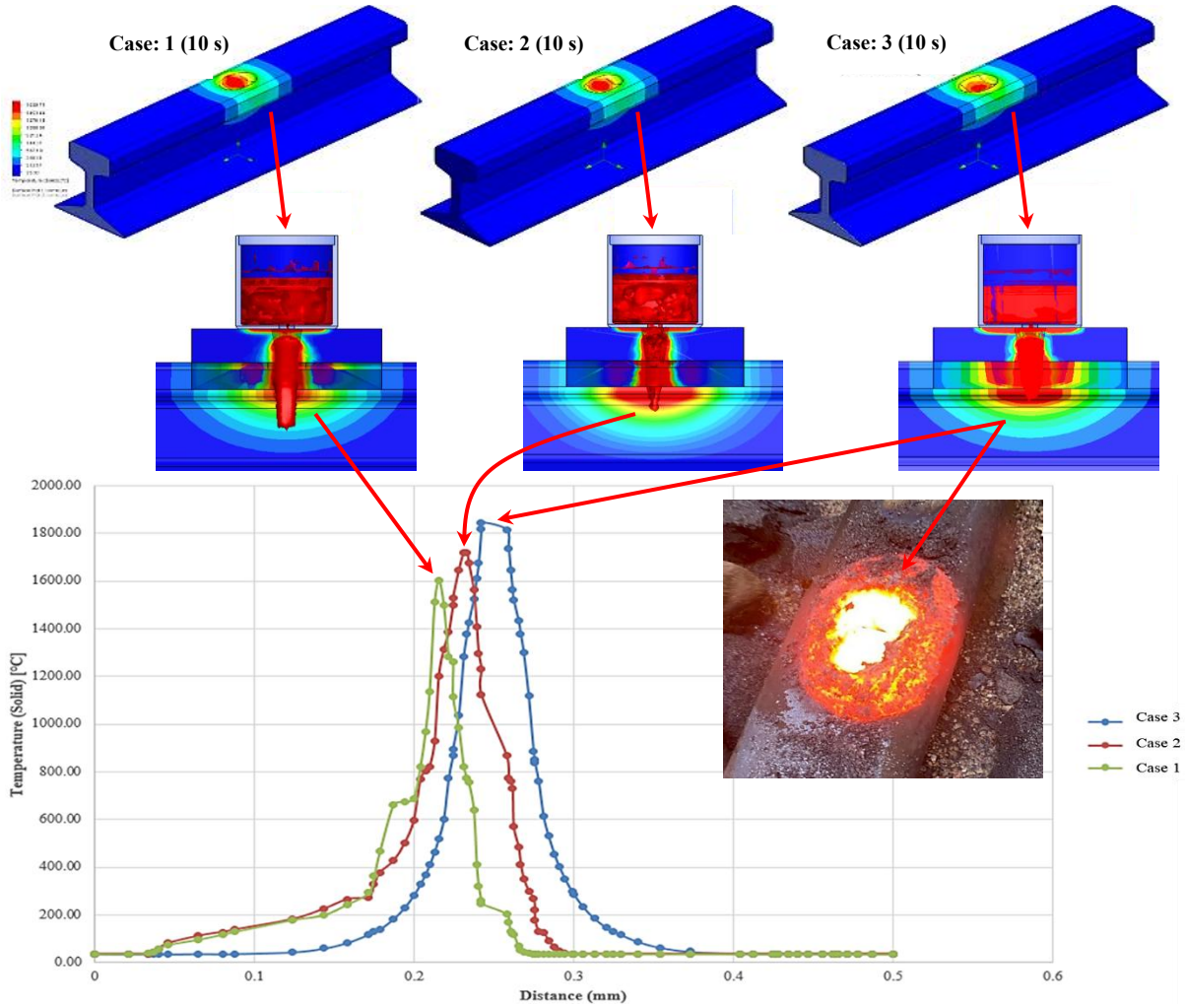

Figure 7. Comparison of temperature distribution across the rail surface obtained from thermal simulation at 10 s.

3.3 Weld surface inspection and correlation with numerical predictions

The correlation between numerical predictions and experimental observations was examined through weld surface inspection and macroscopic analysis for the three mold overflow configurations, as illustrated in Figure 8 and summarized in Table 4. The comparison provides direct validation of the numerical model and clarifies the influence of mold geometry on molten metal flow behavior, heat transfer, and defect formation during thermite-based rail surface repair.

For Case 1 is show in Figure 8(a,d), where the overflow channel was positioned at the outer edge of the wear groove, the numerical simulation predicted a relatively low peak temperature of approximately 1620°C and shallow thermal penetration. These conditions were experimentally confirmed by the observed incomplete melting, irregular weld morphology, and surface oxidation. The limited heat input promoted early development of a mushy zone, which increased momentum damping and restricted molten metal flow, thereby preventing complete metallurgical fusion between the filler metal and the rail substrate [23,24].

In Case 2 is show in Figure 8(b,e), the overflow channel located near the pouring gate resulted in higher peak temperatures in the range of 1750°C to 1800°C and deeper heat penetration, consistent with the numerical temperature field. Although improved melting was achieved, weld surface inspection revealed the presence of porosity concentrated near the central region of the repair zone. This defect formation is attributed to the unbalanced molten metal flow induced by the mold geometry, which led to localized flow instability and insufficient gas evacuation during solidification. These observations are in strong agreement with the predicted non-uniform velocity field and thermal gradients obtained from the coupled thermal–fluid simulation.

Case 3 is show in Figure 8(c,f), exhibited the most favorable weld characteristics among all configurations. The optimized overflow geometry positioned above the pouring gate enabled a stable, gravity-driven molten metal flow, resulting in a uniform velocity field and homogeneous thermal distribution. The numerical model predicted a peak temperature of approximately 1880°C with wide and deep heat penetration, which was experimentally validated by smooth weld morphology, complete groove filling, and the absence of significant porosity or incomplete fusion. The controlled solidification behavior observed in this case confirms the effectiveness of the mold design in promoting balanced heat transfer and continuous molten metal infiltration [23,25].

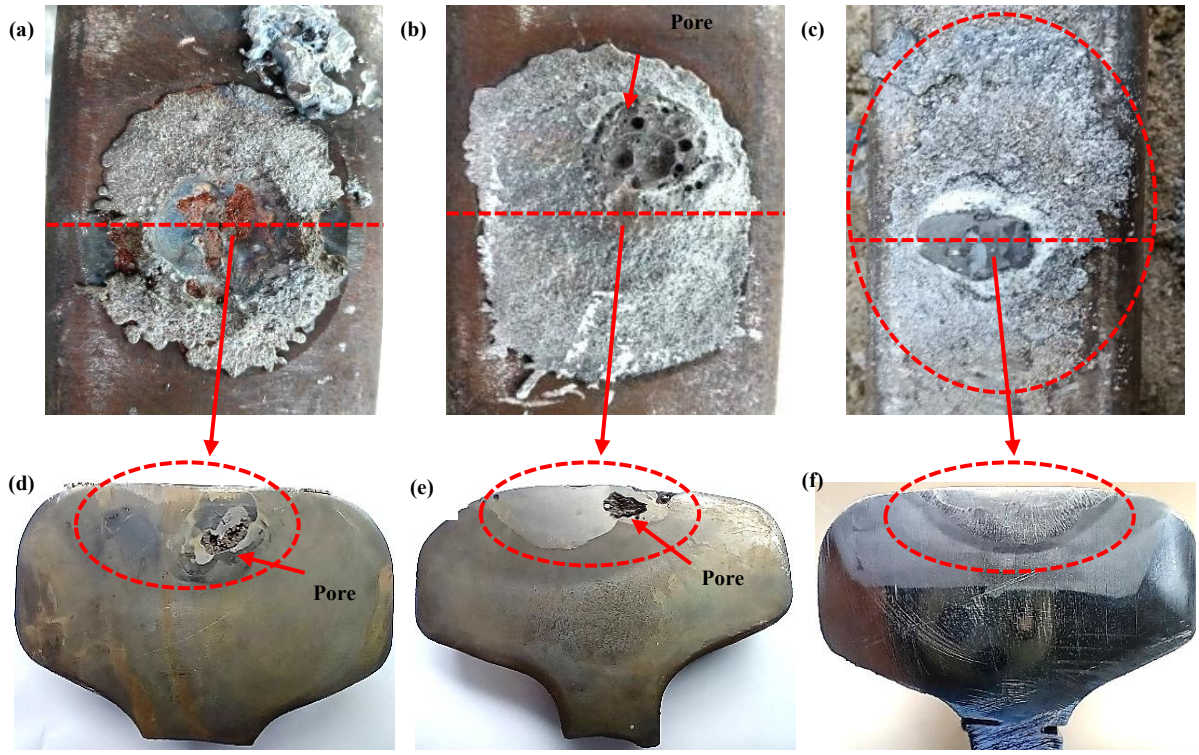

Figure 8. Weld surface inspection of rail repair.

Table 4. Comparative analysis of rail surface repair welding results.

Parameter	Case 1	Case 2	Case 3 (Optimal)
Approx. peak temperature (FEA)	~1620°C	~1750 to 1800°C	~1880°C (stable)
Heat distribution	Narrow and shallow	Deep but localized	Wide and deep, most balanced
Weld surface morphology	Oxidized, porous	Porous with irregular dispersion	Dense, smooth, uniform
Main defects	Incomplete fusion, oxidation	Gas-induced porosity	Negligible
Weld integrity	Low	Moderate	High
Practical applicability	Unsuitable	Usable but risky	Most suitable

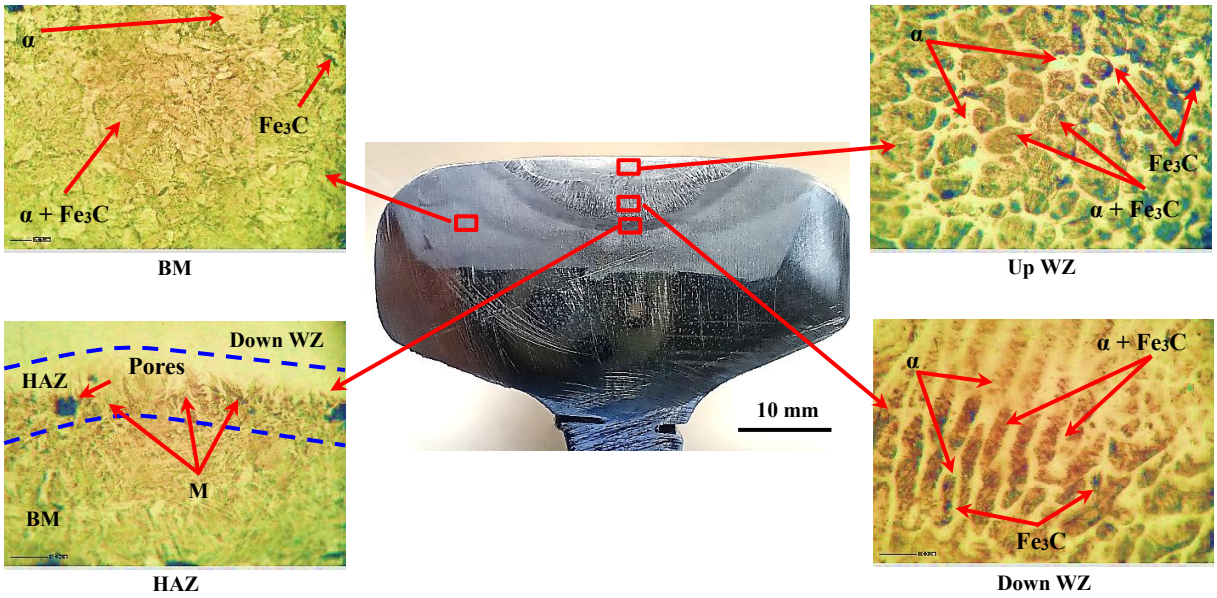

Figure 9. Results of the Macroscopic and Microstructural Examination.

Overall, the experimentally observed weld surface characteristics closely correspond to the numerical predictions, demonstrating that the adopted governing equations and numerical formulation are capable of capturing the key physical mechanisms governing thermite-based rail surface repair. The results clearly indicate that mold overflow configuration strongly influences thermal penetration, molten metal flow stability, and defect formation, with Case 3 providing the optimal balance between heat input, flow behavior, and weld integrity.

3.4 Macroscopic and microstructural examination

The macroscopic and microstructural characteristics of the repaired rail were examined under the optimal processing condition (Case 3), as shown in Figure 9. The results reveal distinct microstructural features in each region of the specimen, while no critical porosity or cracking attributable to the welding process was observed.

The base metal (BM) region exhibited a fine and uniform microstructure consisting predominantly of ferrite (α) and pearlitic ($\alpha + Fe_3C$) distributed throughout the matrix. In the upper weld zone (Up WZ), coarse grains formed as a result of rapid solidification of the filler metal. Isolated small pores were observed, likely caused by air or moisture entrapment within the mold during melting. The microstructure in this region was primarily pearlitic ($\alpha + Fe_3C$), with ferrite (α) cementite (Fe_3C) distributed between lamellae [24-26].

In the lower weld zone (Down WZ), pearlitic grains appeared elongated and aligned along the molten metal flow direction, indicating a slower cooling rate compared with the Up WZ. Small microcracks were detected, which may have originated from residual tensile stresses during solidification or non-uniform shrinkage. Such defects could act as potential initiation sites for fatigue or long-term cracking. In the heat-affected zone (HAZ), coarse grains with a martensitic structure were observed, accompanied by minor porosity. Nevertheless, all detected defects remained within the acceptable limits specified by ISO 5817 [26,27].

4. Conclusions

This study demonstrates that mold design plays a decisive role in controlling heat distribution, molten metal penetration, and weld integrity during thermite-based surface repair of R260 rail steel. Distinct thermal and metallurgical responses were observed among the investigated configurations.

Case 1 generated a maximum temperature of approximately 1620°C with shallow heat dispersion, which resulted in incomplete fusion and surface oxidation due to insufficient thermal penetration. Case 2 achieved higher peak temperatures in the range of 1750°C to 1800°C and deeper penetration; however, its performance was limited by porosity formation caused by unbalanced molten metal flow and inadequate gas evacuation. In contrast, Case 3 exhibited the most favorable behavior, reaching peak temperatures of approximately 1880°C and producing a uniform and deep thermal field that enabled complete groove filling and defect-free weld morphology.

The strong agreement between numerical predictions and experimental observations confirms the reliability of the finite element–based modeling framework in capturing the coupled thermal–fluid phenomena governing thermite welding. Microstructural examination further verified that the optimal configuration (Case 3) produced dense welds with minimal porosity and negligible incomplete fusion, ensuring robust metallurgical bonding.

Overall, Case 3 represents the optimal mold configuration for thermite-based rail surface repair, providing balanced thermal distribution, enhanced weld quality, and improved long-term service reliability. The findings offer practical design guidance for optimizing mold geometry in thermite welding applications and contribute to improving repair efficiency and structural performance in railway maintenance operations. Future investigations should incorporate residual stress analysis to quantify thermally induced stress fields during solidification, as this would further enhance the predictive capability of the model and provide additional insight into the long-term structural performance of the repaired rail.

Acknowledgements

The authors gratefully acknowledge the financial support provided by Phetchabun Rajabhat University. The study also benefited from the facilities and technical assistance made available by the Department of Industrial Engineering Technology and Logistics, Faculty of Agricultural Technology and Industrial Technology, Phetchabun Rajabhat University, the Faculty of Engineering, Rajamangala University of Technology Lanna Phitsanulok, Mueang Phitsanulok, the Faculty of Engineering, Rajamangala University of Technology Lanna, Phitsanulok Campus, and the Faculty of Industrial Education, Rajamangala University of Technology Isan, Khon Kaen Campus. Special appreciation is extended to Mr. Pichai Wattanasrimongkol, Supervising Engineer at the Maintenance Division, State Railway of Thailand (Khon Kaen District), and Assoc. Prof. Dr. Prapas Muangchanburi, Department of Mining and Materials Engineering, Faculty of Engineering, Prince of Songkla University, for their valuable guidance on rail materials and technical support during the experimental analyses. Prince of Songkla University that offers guidance on railway materials and information The data analysis from this investigation is included.

References

[1] M. Akama, "Rolling contact fatigue and wear of rails and wheels: A comprehensive review," *Machines*, vol. 13, no. 10, p. 970, 2025.

[2] S. L. Grassie, "Rolling contact fatigue on the rail head: microscopic observations and mechanical interpretation," *Wear*, vol. 265, no. 9-10, pp. 1212–1223, 2012.

[3] C. Esveld, "MRT selection: a guide to modern railway track design and maintenance," The Netherlands: Esveld, 2001.

[4] D. F. Cannon, K. O. Edel, S. L. Grassie, and K. J. Sawley, "Rail defects: An overview," *Fatigue & Fracture of Engineering Materials & Structures*, vol. 26, no. 10, pp. 865–886, 2003.

[5] H. Z. Oo, and P. Muangjunburee, "Microstructure and wear behavior of repair weld on the flash-butt welded rail," The *Indonesian Journal of Science and Technology*, vol. 11, no. 2, pp. 189–204, 2026

[6] Y. Chen, F. V. Lawrence, C. P. L. Barkan, and J. A. Dantzig, "Heat transfer modelling of rail thermite welding," *Proceedings of the Institution of Mechanical Engineers, Part F: Journal of Rail and Rapid Transit*, vol. 220, no. 3, pp. 207–217, 2006.

[7] S. Kou, "Welding metallurgy," 2nd ed. New York, USA: John Wiley & Sons; 2003.

[8] R. G. Kewalramani, I. Riehl, J. Hantusch, and T. A. Fieback, "CFD model to simulate thermal mould-filling and solid–liquid phase change during aluminothermic welding of rails," in book: Advances in Computational Heat and Mass Transfer, pp. 662–671, 2023.

[9] M. M. Maglio, "Finite element analysis of thermal fields during repair welding of discrete rail defects," Master's thesis. Chalmers University of Technology; 2017.

[10] S. Weiss, I. Riehl, J. Hantusch, and U. Gross, "Numerical investigation on the crucible discharge of steel and slag during the aluminothermic welding process," *Archives of Metallurgy and Materials*, vol. 63, no. 1, pp. 173–180, 2018.

[11] P. K. Sen, M. Bhiwapurkar, and S. P. Harsha, "A 3-D numerical simulation of fatigue crack growth in an alumino thermite welded UIC60 rail joint under different loading conditions," *Materials Today: Proceedings*, vol. 59, pp. 405–412, 2022.

[12] B. Andersson, and B. L. Josefson, "Simulation-based failure analysis of faulty and regulatory railhead repair welding procedures," *Engineering Failure Analysis*, vol. 182, p. 110185, 2025.

[13] European Committee for Standardization. EN 13674-1: Railway applications—Track—Rail—Part 1: Vignole railway rails 46 kg/m and above. Brussels, Belgium: CEN; 2017.

[14] T. DebRoy, H. L. Wei, J. S. Zuback, T. Mukherjee, J. W. Elmer, J. O. Milewski, A. M. Beese, A. Wilson-Heid, A. De, and W. Zhang, "Additive manufacturing of metallic components – process, structure and properties," *Progress in Materials Science*, vol. 92, pp. 112–224, 2018.

[15] Y. Chen, F. V. Lawrence, C. P. L. Barkan, and J. A. Dantzig, "Weld defect formation in rail thermite welds," *Proceedings of the Institution of Mechanical Engineers, Part F: Journal of Rail and Rapid Transi*t, vol. 220, no. 4, pp. 373–384, 2006.

[16] R. W. Fox, A. T. McDonald, and P. J. Pritchard, "Introduction to fluid mechanics," 8th ed. Hoboken, NJ, USA: John Wiley & Sons; 2011.

[17] S. V. Patankar, "Numerical heat transfer and fluid flow," New York, USA: Hemisphere Publishing Corporation; 1980.

[18] V. R. Voller, and C. A. Prakash, "Fixed grid numerical modelling methodology for convection–diffusion mushy region phase-change problems," *International Journal of Heat and Mass Transfer*, vol. 30, no. 8, pp. 1709–1719, 1987.

[19] C. Beckermann, and J. A. Ni, "Volume-averaged two-phase model for transport phenomena during solidification," *Metallurgical and Materials Transactions B*, vol. 22, no. 3, pp. 349–361, 1991.

[20] A. Varma, A. S. Rogachev, A. S. Mukasyan, and S. Hwang, "Combustion synthesis of advanced materials: principles and applications," *Progress in Energy and Combustion Science*, vol. 34, no. 2, pp. 216–285, 2008.

[21] R. B. Bird, R. C. Armstrong, and O. Hassager, "Dynamics of polymeric liquids, vol. 1: fluid mechanics," 2nd ed. New York, USA: John Wiley & Sons; 1987.

[22] F. Campbell, "Complete casting handbook: Metal casting processes, metallurgy, techniques and design," 2nd ed. Oxford, UK: Butterworth-Heinemann; 2015.

[23] S. Chaowakarnkool, K. Uttarasak, S. Jaipayuk, N. Jantaping, and M. Tuiprae, "The effect of Fe–Ni–Mn–Mo high entropy alloy electrode on enhancing the weldability and mechanical properties of railway steel 900A," *Journal of Metals, Materials and Minerals*, vol. 35, no. 1, p. e2292, 2025.

[24] A. Chanpahol, "The study of metallurgical structure of 50-pound railway hard surfacing welding by shielded metal arc welding process," *KKU Research Journal (Graduate Studies),* vol. 19, no. 3, pp. 28–35, 2019.

[25] A. Chanpahol, and B. Kongruang, "Comparative study of H350R and E8016 electrode in surface hard-facing welding

of 100 pound/yard railway by shielded metal arc welding," *Integration Apply Engineering and Industrial Technology*, vol. 12, no. 2, pp. 96–105. 2019;

[26] A. Chanpahol, and S. Srisawad, "Study on microstructure through scanning electron microscope from welding repair of railway surface 70 pound/yard with welding electrodes E110-16G and E1-UM-350," *Pathumthani University Academic Journal*, vol. 11, no. 31, pp. 1–8, 2021.

[27] International Organization for Standardization. ISO 5817: Welding—Fusion-welded joints in steel, nickel, titanium and their alloys—Quality levels for imperfections. Geneva, Switzerland: ISO; 2014.